08,05

Structure and Electronic Transport in $SrIrO_3$ Thin Films Under Epitaxial Strain Induced by Substrate Lattice Mismatch

© N.V. Dubitskiy[1,2], V.A. Baydikova[1,3], A.M. Petrzhik[1], I.E. Moskal[1], A.V. Shadrin[1,4], V.A. Shmakov[1], G.A. Ovsyannikov[1]

[1] Kotelnikov Institute of Radio Engineering and Electronics, Russian Academy of Sciences, Moscow, Russia
[2] National Research University „Higher School of Economics," Faculty of Physics, Moscow, Russia
[3] MIREA — Russian Technological University, Moscow, Russia
[4] Moscow Institute of Physics and Technology (National Research University), Dolgoprudny, Moscow Region, Russia

E-mail: nikita.dubitskiy@gmail.com

Received March 6, 2025
Revised March 6, 2025
Accepted May 5, 2025

Epitaxial strontium iridate ($SrIrO_3$) thin films were fabricated by RF magnetron sputtering on single-crystal substrates: $(110)NdGaO_3$, $(001)SrTiO_3$, $(001)(LaAlO_3)_{0.3}(Sr_2TaAlO_6)_{0.7}$ (LSAT), and $(110)Pb(Mg_{1/3}Nb_{2/3})O_3$-$PbTiO_3$ (PMN-PT). X-ray diffraction techniques were used to investigate structural characteristics and the effect of strain in thin films induced by lattice parameter mismatch between the film and substrate. Analysis of diffraction data reveals changes in the unit cell volume compared to the orthorhombic phase of $SrIrO_3$ crystal in pseudocubic representation. Electronic transport parameters of $SrIrO_3$ thin films exhibit significant dependence on the substrate and deposition conditions. Temperature-dependent resistance analysis revealed the effect of magnetic impurity scattering, attributed to oxygen vacancies, on the electronic transport properties of the films. X-ray photoelectron spectroscopy measurements determined the spin-orbit splitting energy for the Ir $4f$ core level, which varies from 2.99 eV for the $SrIrO_3$ film on $(001)SrTiO_3$ to 3.10 eV for the $SrIrO_3$ film on (110)PMN-PT which correlates with oxygen vacancy concentration, structural perfection, and stoichiometry.

Keywords: $SrIrO_3$ thin films, epitaxial growth, lattice mismatch, oxygen vacancies, electronic transport.

DOI: 10.61011/PSS.2025.06.61710.4HH-25

1. Introduction

Perovskite transition-metal oxides with 5d electrons have attracted significant attention owing to strong spin-orbit coupling, which gives rise to unique electronic states [1,2]. Strontium iridate, $SrIrO_3$, which crystallizes into a monoclinic structure with $a = 0.5604$ nm, $b = 0.9618$ nm, $c = 1.417$ nm (angle $\beta = 93.26°$) at room temperature and ambient pressure [3] is of particular interest. A bulk orthorhombic phase with $a = 0.5597$ nm, $b = 0.5581$ nm, $c = 0.7752$ nm is produced at high temperature 1000 °C and pressure 60 kbar followed by rapid quenching. When $SrIrO_3$ thin films are grown by pulsed-laser deposition on single-crystal substrates at elevated temperatures, epitaxial strain arises due to lattice mismatch between the film and the substrate. A matched substrate is used to produce thin films with a monoclinic structure, which deviates slightly from the orthorhombic one, with $a = 0.56120$ nm, $b = 0.55865$ nm, $c = 0.7934$ nm (angle $\gamma = 90.367°$) [4]. This structure is analyzed accounting for a slight deviation from cubic symmetry and can be represented within a pseudocubic approximation with the lattice parameter $a_c \approx \sqrt{\frac{a^2+b^2}{4}} \approx c/2 = 0.396$ nm [5].

Strong spin-orbit interaction coupled with crystal field leads to splitting t_{2g} of the 5d iridium electron sublevels into states with $J_{eff} = 3/2$ and $J_{eff} = 1/2$ [6]. Structural modifications in $SrIrO_3$ thin films can induce a shift of the Fermi level relative to the band $J_{eff} = 1/2$ [7,8], thereby significantly influencing the electronic properties of the material.

Epitaxial strain resulting from the mismatch of the film and substrate lattice parameters play a key role in forming $SrIrO_3$ thin films [9,10]. For orthorhombic phase of a bulk stoichiometric $SrIrO_3$ crystal in a pseudo-cubic representation with $a_c \approx 0.396$ nm, a lattice cell volume $V_{\text{crystal}} = 62.1 \cdot 10^{-3}$ nm^3 is obtained. Lattice mismatch leads to deformation of the thin film crystal structure followed by a change of interatomic spacings and Ir-O-Ir bond angles [11]. The degree of parameter mismatch between the film and substrate may lead both to compression and expansion of the effective lattice cell volume with respect to an ideal single crystal volume, which affects considerably the electron transport properties of the material [12].

Oxygen vacancies whose concentration depends on the degree of mismatch between the film and substrate lattice parameters plays a crucial role in formation of film proper-

Table 1. Structural parameters of the epitaxial $SrIrO_3$ thin films grown on 4 substrates, interplanar spacings of the films (c_f) and substrates (a_S), degree of film-substrate lattice mismatch (m), effective pseudo-cubic film cell volume (V_{eff}) compared with the pseudo-cubic cell of orthorhombic phase of the $SrIrO_3$ crystal ($V_{crystal} = 62.1 \cdot 10^{-3}$ nm^3)

Sample	c_f, nm	a_S, nm	V_{eff}, 10^{-3} nm^3	m, %
Bulk $SrIrO_3$	0.396	0.396	62.1	–
$SrIrO_3/SrTiO_3$	0.403 ± 0.002	0.390	61.5	3.2
$SrIrO_3/NdGaO_3$	0.404 ± 0.001	0.386	60.4	4.5
$SrIrO_3$/LSAT	0.402 ± 0.001	0.387	60.2	3.9
$SrIrO_3$/PMN-PT	0.394 ± 0.001	0.402	63.5	−1.9

ties [13]. Oxygen mixture composition during sputtering and post-deposition cooling conditions after sputtering are the critical parameters for making epitaxial films that allow the oxygen vacancy concentration to be varied.

Investigation of the influence of epitaxial strain on the properties of $SrIrO_3$ thin film properties is of particular interest when using a wide range of substrates with various lattice parameters. In particular, a ferroelectric $Pb(Mg_{1/3}Nb_{2/3})O_3$-$PbTiO_3$ substrate provides additional opportunities for film tension control [14].

2. $SrIrO_3$ film sputtering technique

$SrIrO_3$ thin films were produced by the RF magnetron sputtering method [15,16]. Preliminary evacuation was performed up to $2 \cdot 10^{-5}$ mbar. $SrIrO_3$ films were grown using single-crystal substrates similar with the single-crystal $SrIrO_3$ phase in terms of lattice parameters: (110)$NdGaO_3$ (NGO), (001)$SrTiO_3$ (STO), (001)$(LaAlO_3)_{0.3}(Sr_2TaAlO_6)_{0.7}$ (LSAT) and (110)$Pb(Mg_{1/3}Nb_{2/3})O_3$-$PbTiO_3$ (PMN-PT). Pressed powder mixed in the $SrIrO_3$ ratio and annealed at 1000 °C was used as a target. The X-ray diffraction analysis confirmed single-phase structure of the targets. For the growth of $SrIrO_3$ films, the NGO, STO and LSAT substrates were heated to 770 °C, and the PMN-PT substrates were heated to 750 °C, to ensure better and uniform heating, the substrates were attached to a heater using silver paste, which facilitated the epitaxial growth of $SrIrO_3$ thin films.

$SrIrO_3$ film sputtering took place at 0.25 mbar, at this pressure the resulting films had the closest lattice parameters to the literature data concerning single crystals and thin films. In addition, these films exhibited a metallic temperature dependence [17] of resistance, while an increase in pressure led to a substantial rise in the film resistance. Operating pressure in the chamber consisted of the 10/35 Ar and O_2 mixture and was used to grow $SrIrO_3$ films without forming the Sr_2IrO_4 or $Sr_3Ir_2O_7$crystals [18,19].

The samples were annealed in two stages. During the first stage, the films were cooled to 500 °C immediately after sputtering and annealed in oxygen for 30 minutes. The second stage consisted in slow cooling of the film to room temperature in oxygen, the cooling rate was 10 degrees per minute. At 50 W and 0.25 mbar, the growth rate was about 10 nm/h to produce 30 nm films during 3 hour sputtering.

3. $SrIrO_3$ film structure

Structural properties of the $SrIrO_3$ films were investigated by the X-ray diffraction method using the Rigaku SmartLab rotating copper anode diffractometer. Measurements were performed in a parallel beam configuration with Ge(220)×2 monochromator at Cu$K_{\alpha 1}$ ($\lambda = 1.54056$ Å). Epitaxial growth of the $SrIrO_3$ films was confirmed by transmission microscopy (TEM) data [20]. For example, for the $SrIrO_3$ film sputtered onto a (001)$SrTiO_3$ substrate, the epitaxial ratio is as follows (001)$SrIrO_3$//(001)$SrTiO_3$, [100]$SrIrO_3$//[100]$SrTiO_3$, i. e. cube-on-cube growth takes place. A more complex type of growth takes place when the $SrIrO_3$ film is sputtered onto (110)$NdGaO_3$ or (110)PMN-PT substrates.

XRD patterns (Figure 1) reveal the dependence of the film interplanar spacing on the substrate lattice parameters. Intense and distinct reflections (00k) ($k = 1, 2, 3, 4$) are observed for the (001)$SrTiO_3$, (001)LSAT and (110)$NdGaO_3$ substrates (Figure 1), at the same time (nm0)$SrIrO_3$ reflections were observed for a film deposited onto the (110)PMN-PT substrate (Figure 2).

Lattice parameter review of the epitaxial $SrIrO_3$ films revealed considerable dependence of the lattice parameters on the substrate (Table 1). Films on the (001)$SrTiO_3$, (001)LSAT and (110)$NdGaO_3$ substrates demonstrate compression ($m = c/a - 1 = 3.2{-}4.5\,\%$) followed by an increase in interplanar spacing of the film lattice cell c to 0.402−0.404 nm [21] with simultaneous decrease in the substrate-defined parameter a to 0.387−0.391 nm. The $SrIrO_3$ film on the $SrTiO_3$ substrate [22] is of particular interest because, despite of a significant mismatch of the lattice parameters ($m = 3.2\,\%$), it demonstrates a pseudo-cubic cell volume $V_{eff} = 61.5 \cdot 10^{-3}$ nm^3, which is the closest to the orthorhombic phase cell volume of the $SrIrO_3$ crystal ($V_{crystal} = 62.1 \cdot 10^{-3}$ nm^3).

For the film on PMN-PT (Figure 2, *a*), there is tension in the substrate plane ($m = -1.9\,\%$) with $a = 0.402$ nm,

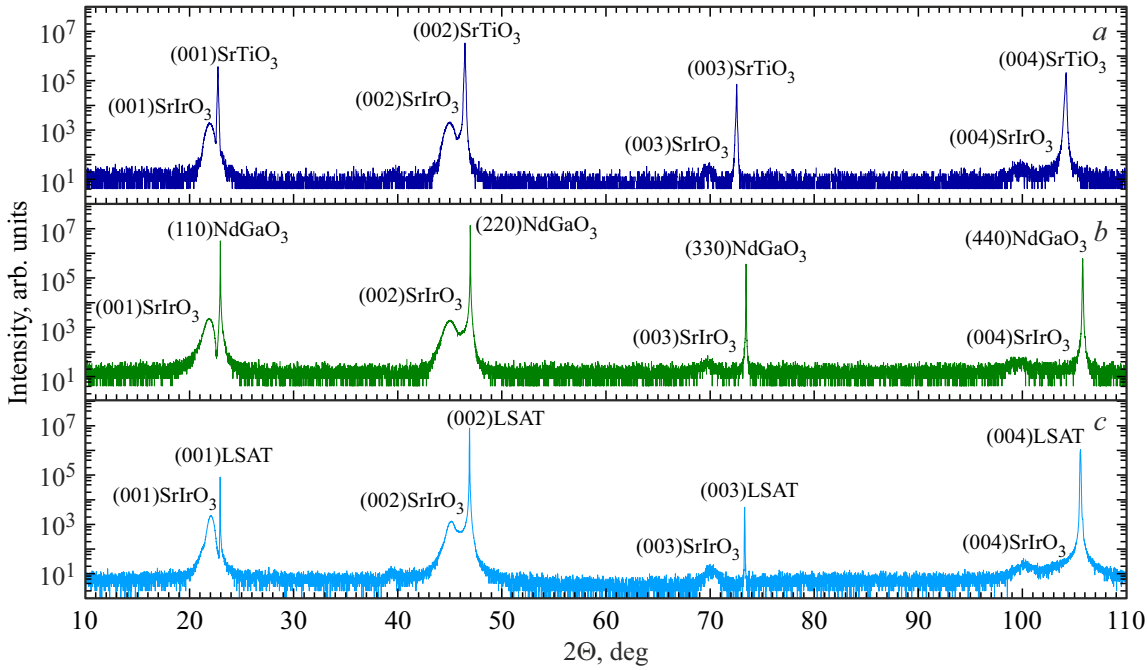

Figure 1. X-ray Bragg reflection diffraction patterns of epitaxial $SrIrO_3$ thin films grown on substrates: (*a*) — $(001)SrTiO_3$, (*b*) — $(110)NdGaO_3$, (*c*) — $(001)(LaAlO_3)_{0.3}(Sr_2TaAlO_6)_{0.7}$.

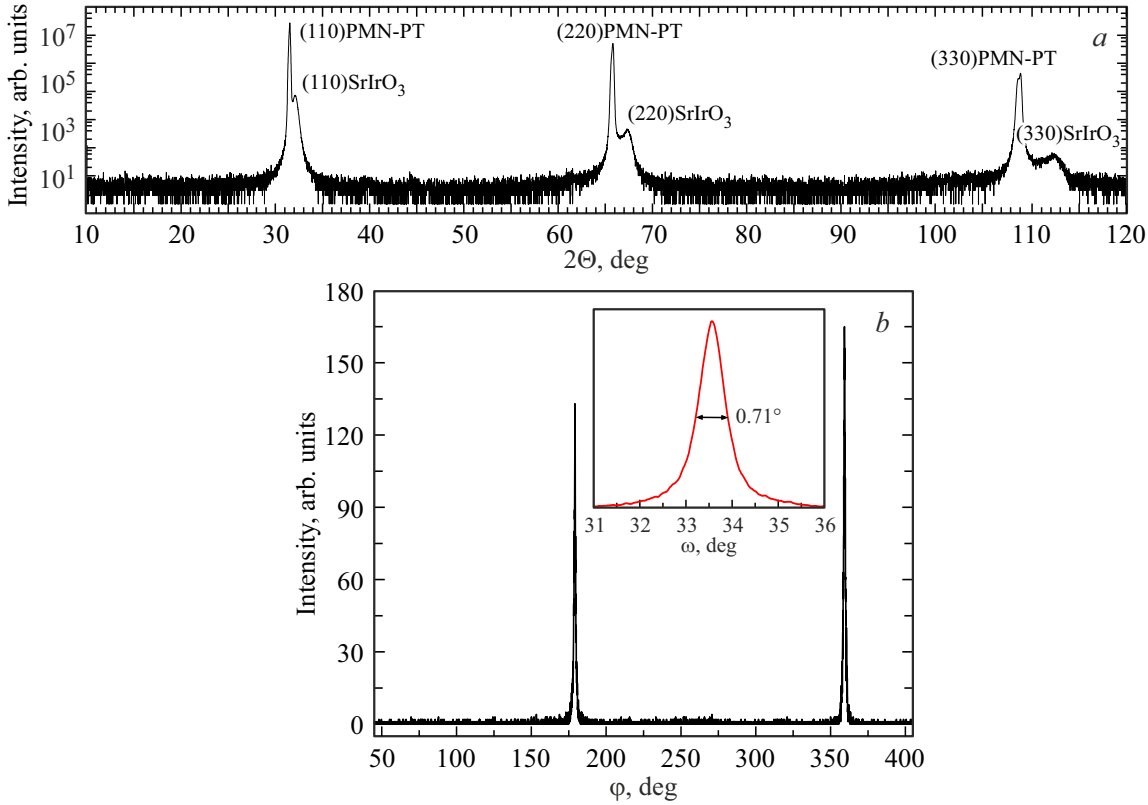

Figure 2. (*a*) X-ray Bragg reflection diffraction pattern of the epitaxial $SrIrO_3$ thin film grown on the PMN-PT substrate. (*b*) φ-scan of the $SrIrO_3$ film, the inset shows the rocking curve (ω-scan) of the $(220)SrIrO_3$ reflection. FWHM of the rocking curve is 0.71°.

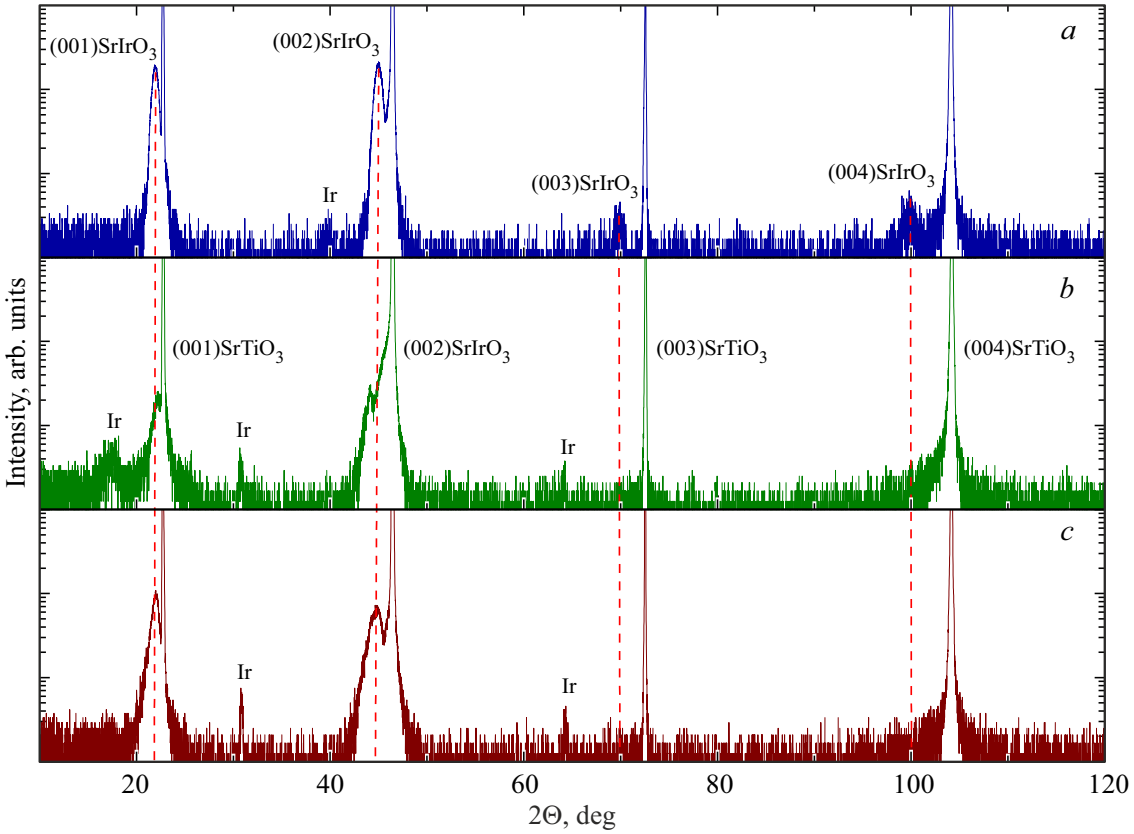

Figure 3. X-ray diffraction patterns of the $SrIrO_3$ thin films grown on the $SrTiO_3$ substrates with argon/oxygen ratio of 10/35 and mixture pressure of: (a) $P_{Ar/O_2} = 0.25$ mbar, (b) 0.5 mbar, (c) 0.75 mbar.

which leads to an increase in V_{eff} to $63.5 \cdot 10^{-3}$ nm^3 compared with $V_{crystal}$ [23].

Before each recording of symmetric $2\Theta/\omega$ scans, rocking curves and φ-scans, mandatory alignment of sample position was performed, including Z-scan (vertical position), R_x-scan (sample table rocking along the source-detector direction) and R_y-scan (sample table rocking perpendicular to the beam). Alignment was performed using the most intense substrate peak (200) or (220).

To determine ordering in the substrate plane, φ-scan was recorded for the (110)$SrIrO_3$ film grown on the (110)PMN-PT substrate (Figure 2, b), and the angle χ was preset to 45° (assuming that $\chi = 0°$ is the table position in the floor plane). Observed distinct reflections with $\varphi \approx 180°$ and $\varphi \approx 360°$ (with angular separation of 180°) and FWHM of peaks $1.1 \pm 0.1°$ indicate the formation of an epitaxial film with a single in-plane epitaxial orientation in the substrate plane. According to the reciprocal space map projection for the (011) orientation in the cubic crystal, the (100) and (010) planes shall be observed at $\chi = 45°$, and the (001) and $(00\bar{1})$ planes shall be observed at $\chi = 90°$. Thus, the presence of only two reflections in φ-scanning at $\chi = 45°$ confirms the only orientation option of $SrIrO_3$ in the substrate plane.

Analysis of the rocking curve of the (220) $SrIrO_3$ reflection revealed a well-defined diffraction peak with FWHM, 0.71° (inset in Figure 2, b) indicating a high degree of out-of-plane texture (low mosaicity) in the film despite the significant lattice mismatch between $SrIrO_3$ and the PMN-PT substrate.

To determine the influence of growth conditions on the structural parameters of films grown on the $SrTiO_3$ substrate, dependencies of crystal parameters on the pressure of Ar/O_2 mixture with a ratio of 10/35. X-ray diffraction analysis of the $SrIrO_3$ films (Figure 3) shows that single-phase epitaxial $SrIrO_3$ films with typical (00l) reflections are formed for all three samples. Low peaks of metallic iridium are observed and their intensity varies depending on the growth conditions. $SrIrO_3$ film grown at 0.25 mbar (Figure 3, a) demonstrates $c = 0.403$ nm and $V_{eff} = 61.45 \cdot 10^{-3}$ nm^3. Increase in pressure to 0.5 mbar (Figure 3, b) leads to the growth of c to 0.407 nm with a simultaneous decrease in the cell volume to $61.15 \cdot 10^{-3}$ nm^3. Further increase in pressure to 0.75 mbar (Figure 3, c) is accompanied by a small decrease in c to 0.405 nm and increase in the effective cell volume to $61.76 \cdot 10^{-3}$ nm^3.

Dependence of c on the total gas mixture pressure is nonmonotonic with a maximum for the $SrIrO_3$ films at $P_{Ar/O_2} = 0.5$ mbar. Parameter m shows a monotonic increase as the pressure grows from 3.2% at $P_{Ar/O_2} = 0.25$ mbar to 3.7% at $P_{Ar/O_2} = 0.75$ mbar.

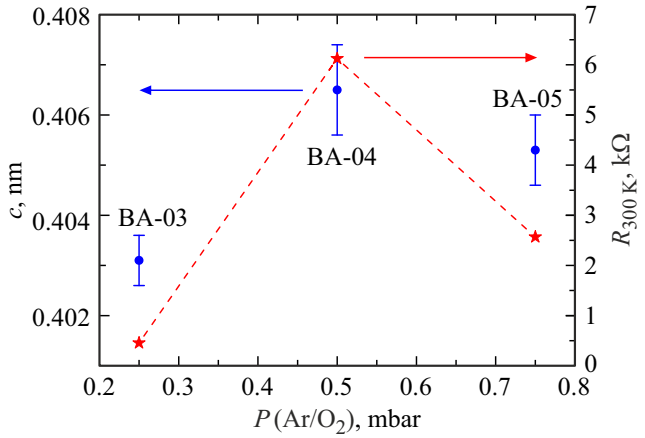

Figure 4. Dependence of the lattice cell parameter (filled circles) on gas mixture pressure P_{Ar/O_2} ($Ar/O_2 = 10/35$) for the investigated epitaxial $SrIrO_3$ thin films grown on the $SrTiO_3$ substrates: 0.25 mbar (BA-03), 0.5 mbar (BA-04), 0.75 mbar (BA-05). Points corresponding to the resistance of these samples at 300 K are marked with asterisks.

4. Atomic-force microscopy of the $SrIrO_3$ films

Surface morphology of the $SrIrO_3$ thin films grown on various substrates was investigated by the atomic-force microscopy (AFM) method. Sample surface images were made in a semi-contact mode using the Solver PRO M (NT MDT) scanning probe microscope. This microscope provides a resolution up to 1 nm and is used to examine samples with dimensions up to $12 \times 12 \times 2$ mm, positioning resolution is 5 μm.

Figure 5, *a* shows the AFM image of the $SrIrO_3$ film grown on the $SrTiO_3$ substrate. Topographic scan with dimensions $5 \times 5\,\mu m^2$ demonstrates a granular structure with quasi-regular distribution of texture features. Roughness along the line marked in the image (Figure 5, *b*) shows typical variations in a nanometer range that achieve the maximum peak-to-peak height of 15.93 nm. RMS roughness of this $SrIrO_3$ film is $RMS = 1.44$ nm.

Additional statistical parameters obtained from the height distribution review indicate high quality of the $SrIrO_3$ film on the $SrTiO_3$ substrate [24]. Near-zero skewness (0.001) indicates a symmetric height distribution with respect to the mean surface plane. Kurtosis is 3.18, which corresponds to a near-normal Gaussian distribution of heights and is typical of evenly formed epitaxial layers.

The same investigations were carried out for samples grown on the NGO, LSAT and PMN-PT substrates. Film on the NGO substrate exhibited the RMS roughness ($RMS = 1.44$ nm) similar to that of $SrTiO_3$, but a larger peak-to-peak height (25.58 nm) and a higher kurtosis (4.98), which indicates that there are more pronounced local texture features.

$SrIrO_3$ film grown on the LSAT substrate exhibited the lowest RMS roughness among all samples (0.31 nm), however, statistical analysis revealed anomalously high skewness (11.00) and kurtosis (495.22). Such data indicates that there are individual high peaks on predominately smooth surface, which may be due to substrate defects or specifics of the growth process [25].

$SrIrO_3$ film on the PMN-PT substrate is characterized by the highest roughness ($RMS = 6.11$ nm) and maximum peak-to-peak height (47.01 nm) among the studied systems. A small negative skewness (−0.22) indicates a small predominance of valleys over peaks in the surface structure.

The investigations show that morphological properties of the $SrIrO_3$ films depend on the selected substrate. Samples on the $SrTiO_3$ and $NdGaO_3$ substrates demonstrate comparable roughness, however, the film on $SrTiO_3$ is characterized by more uniform distribution of texture features and, consequently, by higher structural perfection. The sample on LSAT, despite the lowest roughness, has a statistically inhomogeneous surface with individual protruding defects. The film on PMN-PT has a more developed surface texture,

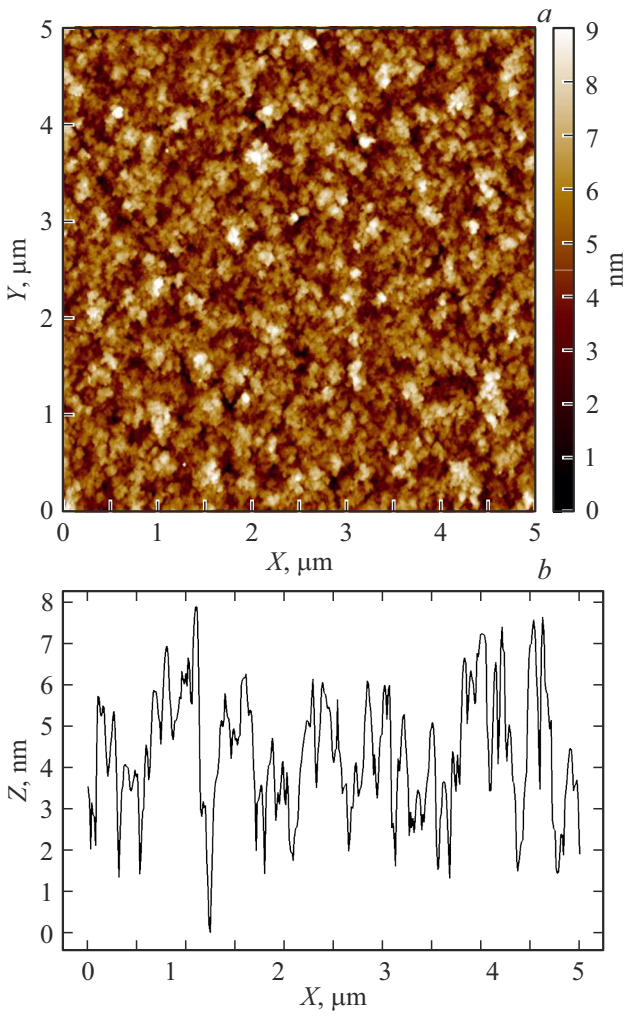

Figure 5. (*a*) AFM image of the surface of the epitaxial $SrIrO_3$ film grown on the $SrTiO_3$ substrate. Scanning area dimensions are $5 \times 5\,\mu m^2$. (*b*) Horizontal elevation profile curve $Y = 1\,\mu$m in the AFM image.

which may be due to structural mismatch between the substrate and growing layer.

AFM surface morphology analysis suggests that the $SrTiO_3$ substrate provides the best growth conditions for high quality epitaxial $SrIrO_3$ films with uniform surface morphology.

5. Electronic transport characteristics

Electronic transport measurements of the $SrIrO_3$ films employed the four-probe Montgomery method in the temperature range of 77−300 K [26]. For all samples, an identical square configuration with the same dimensions and contact layout was used to ensure proper comparison without additional geometrical corrections. Figure 6 shows the temperature dependencies of the sheet resistance for three mixture pressures at $P_{Ar/O_2} = 0.25$, 0.5 and 0.75 mbar.

The $SrIrO_3$ film (BA-03, 0.25 mbar) demonstrates a monotonic decrease in resistance from 0.45 kΩ at 300 K to 0.39 kΩ at 77 K. For the $SrIrO_3$ film (BA-04, 0.5 mbar), resistance increases with temperature decrease from 6.0 kΩ at 300 K to 9.5 kΩ at 77 K [27]. The $SrIrO_3$ film (BA-05, 0.75 mbar) shows an increase in resistance from 2.5 kΩ at 300 K to 3.0 kΩ at 77 K. The observed difference in the conductivity behavior and absolute resistance values is associated with oxygen vacancy variation in the $SrIrO_3$ films [28].

Temperature dependencies of the sheet resistance of epitaxial $SrIrO_3$ thin films on 4-substrates normalized to a value at room temperature are shown in Figure 7. The shape of $R(T)$ curves depends significantly on the type of substrate to be used [29,30]. All films demonstrate a metallic type of conductivity ($dR/dT > 0$) at high temperatures within

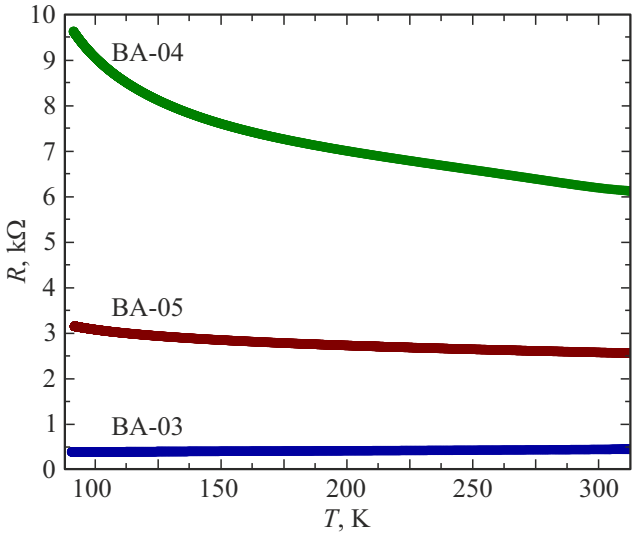

Figure 6. Temperature dependence of the sheet resistance of the $SrIrO_3$ films grown on the $SrTiO_3$ substrates at different gas mixture pressures P_{Ar/O_2} ($Ar/O_2 = 10/35$): 0.25 mbar (BA-03), 0.5 mbar (BA-04), 0.75 mbar (BA-05).

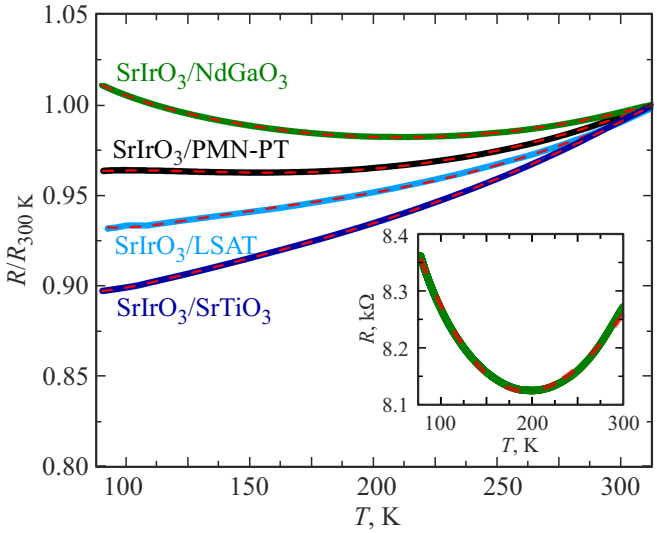

Figure 7. Dependences of the normalized resistance on temperature, approximations according to equation (1) are shown dashed. The inset shows the dependence of squared resistance of the $SrIrO_3$ film grown on the $NdGaO_3$ substrate, with approximation according to equation (1).

300−200 K, followed by an upturn ($dR/dT < 0$) upon further cooling.

Experimental temperature-resistance dependencies of the $SrIrO_3$ films $R(T)$ were analyzed within the following model [31]:

$$R(T) = R_0 + R_1\left(\frac{T}{T_M}\right)^B + R_K\left(\frac{T_K^*}{T^2 + T_K^*}\right)^S, \qquad (1)$$

where R_0 is the resistance induced by impurities (independent of temperature), the second term R_1 is a parameter describing the contribution of electron-phonon interaction. R_K characterizes the contribution of electron scattering on the localized magnetic moments, $T_K^* = \sqrt{\frac{T_K}{2^{1/S}-1}}$. $S = 0.43$ [32] defines the interaction between localized spins and conductivity electrons, $B = 1.44$ defines the power-law temperature dependence of electron-phonon scattering on temperature, T_M is the normalizing temperature.

Table 2 shows electrophysical parameters for all films. It can be seen that T_K differs considerably for films on different substrates: from 9.6 K for $SrIrO_3/SrTiO_3$ to 556 K for $SrIrO_3$/LSAT, the high value of T_K arises from a breakdown of the perturbative regime used in for model (1) [33]. The strongest effect of magnetic impurities (maximum value is $R_K = 2225\,\Omega$) is observed in films on the $NdGaO_3$ substrate. By contrast, the film on PMN-PT demonstrates the minimum value $R_K = 3.2\,\Omega$, which agrees with the lowest degree of lattice mismatch $m = -1.9\,\%$.

Contribution of the electron-phonon interaction characterized by R_1 also shows a significant variation: from 0.6 Ω for $SrIrO_3$ on $NdGaO_3$ to $5 \cdot 10^{-3}\,\Omega$ for $SrIrO_3$ on PMN-PT. This difference may be associated with the phonon scattering variation resulting from lattice deformation.

Table 2. Electrophysical parameters of epitaxial $SrIrO_3$ thin films grown on the: $SrTiO_3$, $NdGaO_3$, LSAT and PMN-PT substrates

Sample	T_K, K	R_K, Ω	R_0, Ω	R_1, Ω	T_M, K
$SrIrO_3/SrTiO_3$	9.6	1268	5965	0.3	1.04
$SrIrO_3/NdGaO_3$	253	2225	6258	0.6	İ.62
$SrIrO_3$/LSAT	556	10.6	2.5	0.05	13.68
$SrIrO_3$/PMN-PT	459	3.7	1.9	0.005	5.79

Table 3. XPS spectra parameters of the epitaxial $SrIrO_3$ thin films grown on the: $SrTiO_3$, $NdGaO_3$, LSAT and PMN-PT substrates

Sample	Sr, %	Ir, %	Sr/Ir	Ir(B)/Ir(A)	ϵ_{SO}, eV
$SrIrO_3/SrTiO_3$	53.81	46.19	1.16	1.20	3.03
$SrIrO_3/NdGaO_3$	56.28	43.72	1.29	1.14	2.99
$SrIrO_3$/LSAT	56.94	43.06	1.32	1.35	2.99
$SrIrO_3$/PMN-PT	57.77	42.23	1.37	1.20	3.10

The observed patterns indicate the defining role of structural deformations in formation of electronic properties of the $SrIrO_3$ films. Epitaxial strain induced by the lattice mismatch lead to electron structure modifications and, consequently, to conductivity variation.

6. Chemical and electronic structure analysis by the X-ray photoelectron spectroscopy method

Chemical and electronic structures of the $SrIrO_3$ films were analyzed by X-ray photoelectron spectroscopy (XPS). Shifts of the binding energy photoelectron lines are used to examine the change in the chemical environment of atoms with high accuracy. This study used the Theta Probe (Thermo Fisher Scientific, UK) spectrometer at a residual gas pressure at least $1.3 \cdot 10^{-8}$ mbar. A standard AlKα anode with the emitted photon energy $E = h\nu = 1486.6$ eV was used for X-ray generation. Absolute spectrometer resolution on the Ag $3d_{5/2}$ line was 0.46 eV. X-ray photon beam size was set to 400 μm energy analyzer was in the FAT (Fixed Analyzer Transmission) mode during all measurements. The absolute uncertainty of the photoelectron kinetic energy did not exceed 0.1 eV. Measurements were conducted in two stages. The first stage measured the panoramic spectrum of the film with photoeletron's kinetic energy interval equal to 1 eV, while the photoelectron pass energy of the spectrometer energy analyzer was set to 200 eV. The second stage included the measurement of detailed spectra of individual photoelectron energy ranges corresponding to Sr and Ir with the photoelectron energy interval equal to 0.1 eV, spectrum analyzer pass energy was set to 50 eV.

Panoramic spectrum of the $SrIrO_3$ film is shown in Figure 8, *a*. Ir $4f$ spectrum consists of two components: Ir $4f_{7/2}$ and Ir $4f_{5/2}$ induced by spin-orbit interaction (Figure 8, *b*). Spin-orbit splitting ϵ_{SO} between these components for the $SrIrO_3$ film on $NdGaO_3$ is 2.99 eV, on $SrTiO_3$ is 3.03 eV, on LSAT is 2.99 eV, on PMN-PT is 3.10 eV (Table 3). The obtained data are in good agreement with the literature data for $SrIrO_3$ ($\epsilon_{SO} \sim 3.0$ eV) [34]. Such spin-orbit splitting values are typical of iridium with oxidation state Ir^{4+} [35].

It is important that the magnitude of spin-orbit splitting depends considerably on the electronic structure and defects in the material. As shown in [28], ϵ_{SO} is sensitive to the concentration of oxygen vacancies in the $SrIrO_3$ films. $SrIrO_3$ films with high ϵ_{SO} are generally characterized by a lower concentration of oxygen vacancies and, therefore, by more perfect stoichiometry and structure. In this context, the observed maximum splitting ($\epsilon_{SO} = 3.10$ eV) for the $SrIrO_3$ film on the PMN-PT substrate may indicate the best oxygen stoichiometry and a lower concentration of magnetic impurities compared with other test samples.

For more detailed analysis of the electronic structure, each of the spin-orbit components Ir $4f_{7/2}$ and Ir $4f_{5/2}$ was approximated by two components denoted as Ir(A) and Ir(B) that correspond to iridium atoms with various local distortions of oxygen octahedra. Peak intensity ratio Ir(B)/Ir(A) varies from 1.14 to 1.35 for different substrates [36], which is indicative of different distribution of these states. The ratio of Sr to Ir varies from 1.16 ($SrIrO_3/SrTiO_3$) to 1.37 ($SrIrO_3$/PMN-PT). Such values are due to different lattice parameters and degree of mismatch between the film and substrate measured from the X-ray diffraction analysis.

Sr $3d$ peaks also demonstrate a doublet structure (Sr $3d_{5/2}$ and Sr $3d_{3/2}$) with typical splitting about 1.8 eV, which corresponds to Sr in the oxide environment (Figure 8, *c*).

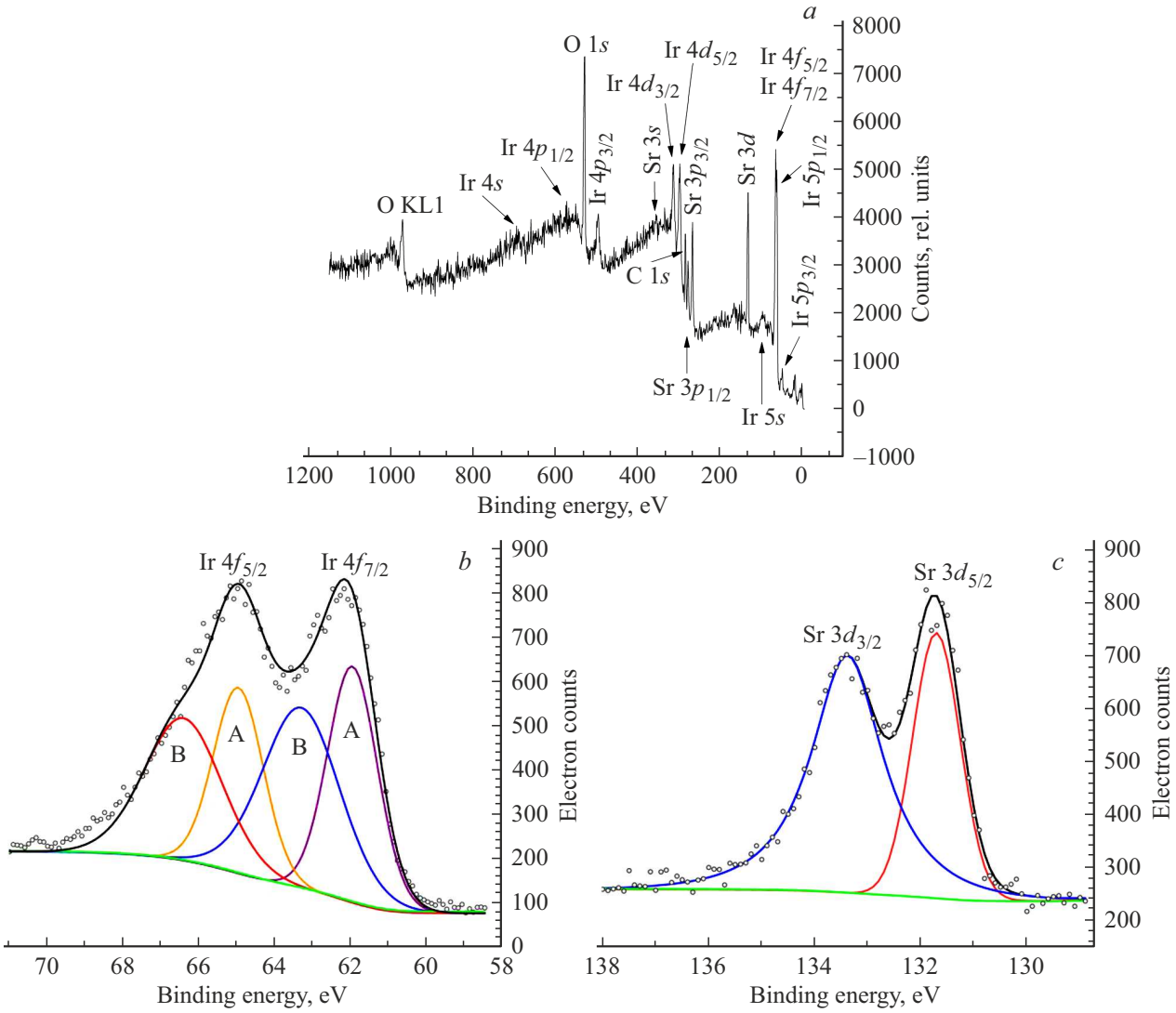

Figure 8. (*a*) — Panoramic photoelectronic spectrum of an $SrIrO_3$ film grown on the (001)$SrTiO_3$ substrate is presented. The arrows indicate the peak positions corresponding to the binding energies of the electrons in various sublevels of the electron shells of the chemical elements contained in the film. Approximate values of energy levels for peak identification (belonging to an element and sublevel) are determined from XPS NIST Database. (*b*) — XPS spectrum of the binding energy range for the electronic sublevel of $4f$ iridium. Orange Ir(A) $4f_{5/2}$ and red Ir(B) $4f_{5/2}$ and lines — two components of approximation by Voigt peak functions Ir $4f_{7/2}$. Purple Ir(A) $4f_{7/2}$ and blue Ir(B) $4f_{7/2}$ lines — two components of the peak approximationIr $4f_{7/2}$. (*c*) — Detailed XPS spectrum of the binding energy range for the electronic sublevel of $3d$ strontium. Red line — approximation the peak is Sr $3d_{5/2}$. Blue line — approximation of the peak Sr $3d_{3/2}$. In Figures (*b*) and (*c*), the dots indicate the experimental characteristic measured by the spectroscope. Green line — background caused by inelastic scattering of photoelectrons in a film, determined by the Shirley method. Black line — approximation of the measured data.

7. Conclusion

The study investigated structural, electronic and transport properties of epitaxial $SrIrO_3$ thin films grown by the high-frequency magnetron sputtering method on single-crystal substrates: (110)$NdGaO_3$, (001)$SrTiO_3$, (001)$(LaAlO_3)_{0.3}(Sr_2TaAlO_6)_{0.7}$ (LSAT) and (110)$Pb(Mg_{1/3}Nb_{2/3})O_3$-$PbTiO_3$ (PMN-PT). Structural analysis showed that all grown films were close to the pseudo-cubic phase. The degree of lattice mismatch between the film and substrate was found to vary from $-1.9\,\%$ for PMN-PT to $4.5\,\%$ for $NdGaO_3$ leading to various degrees of crystal structure deformation. Effective lattice cell volume of the $SrIrO_3$ films, except the sample on the PMN-PT substrate, is smaller than the pseudo-cubic cell volume of the orthorhombic phase of $SrIrO_3$ crystal ($62.1 \cdot 10^{-3}$ nm^3), which indicates that a squeezed crystal structure is formed.

Electrical transport measurements revealed metallic conductivity in the $SrIrO_3$ film, followed by a resistance upturn at low temperatures. Analysis of the temperature-resistance dependence within a simplified model taking into account

the influence of electron scattering on magnetic impurities showed that a type of substrate had a considerable influence on the electronic transport of the $SrIrO_3$ films. T_K characterizing the interaction with magnetic impurities varies from 253 K for the film on $NdGaO_3$ to 556 K for the film on LSAT, which is associated with the degree of lattice deformation. The XPS examination was used to measure the atomic composition of the $SrIrO_3$ films and to investigate the electronic structure and chemical sate of iridium and strontium ions, in addition, spin-orbit splitting was evaluated and was about 3 eV for Ir $4f$ states, which is typical for Ir^{4+} in the octahedral environment. Ir(B)/Ir(A) demonstrates the dependence on the type of substrate, which agrees with various degrees of lattice deformation. The findings demonstrate the leading role of substrate in formation of structural and electronic properties of the $SrIrO_3$ thin films, which offers opportunities for targeted modification of the functional characteristics of the films by choosing a particular substrate.

Funding

The study was performed at the cost of grant No. 23-79-00010 provided by the Russian Science Foundation, https://rscf.ru/project/23-79-00010/ using the equipment provided by the Shared Research Facility of unique nanotechnology research equipment (Shared Research Facility of Moscow Institute of Physics and Technology).

Conflict of interest

The authors declare that they have no conflict of interest.

References

[1] S. Sardar, M. Vagadia, T.M. Tank, J. Sahoo, D.S. Rana. J. Appl. Phys. **135**, 8 (2024).
[2] H. Chen, D. Yi. APL Mater. **9**, 6 (2021).
[3] J.M. Longo, J.A. Kafalas, R.J. Arnott. J. Solid State Chem. **3**, *2*, 174 (1971).
[4] J. Liu, D. Kriegner, L. Horak, D. Puggioni, C. Rayan Serrao, R. Chen, D. Yi, C. Frontera, V. Holy, A. Vishwanath, J.M. Rondinelli, X. Marti, R. Ramesh. Phys. Rev. B **93**, *8*, 085118 (2016).
[5] B.L. Chamberland, A.R. Philpotts. J. Alloys Compd. **182**, *2*, 355 (1992).
[6] G. Cao, P. Schlottmann. Rep. Prog. Phys. **81**, *4*, 042502 (2018).
[7] S.J. Moon, H. Jin, K.W. Kim, W.S. Choi, Y.S. Lee, J. Yu, T.W. Noh. Phys. Rev. Lett. **101**, *22*, 226402 (2008).
[8] Z.T. Liu, M.Y. Li, Q.F. Li, J.S. Liu, W. Li, H.F. Yang, D.W. Shen. Sci. Rep. **6**, *1*, 30309 (2016).
[9] J.H. Gruenewald, J. Nichols, J. Terzic, G. Cao, J.W. Brill, S.S.A. Seo. J. Mater. Res. **29**, *21*, 2491 (2014).
[10] L. Horák, D. Kriegner, J. Liu, C. Frontera, X. Marti, V. Holý. J. Appl. Crystallogr. **50**, *2*, 385 (2017).
[11] B. Kim, B.H. Kim, K. Kim, B.I. Min. Sci. Rep. **6**, *1*, 27095 (2016).
[12] I.E. Moskal, A.M. Petrzhik, Yu.V. Kislinskii, A.V. Shadrin, G.A. Ovsyannikov, N.V. Dubitskiy. Bulletin of the Russian Academy of Sciences: Physics. **88**, *4*, 581 (2024).
[13] V. Fuentes, L. Balcells, Z. Konstantinović, B. Martínez, A. Pomar. Nanomaterials **14**, *3*, 242 (2024).
[14] S.S. Li, Y. Zhang, J.S. Ying, Z.C. Wang, J.M. Yan, G.Y. Gao, R.K. Zheng. J. Appl. Phys. **133**, 1 (2023).
[15] I.E. Moskal, Yu.V. Kislinskii, A.M. Petrzhik, G.A. Ovsyannikov, N.V. Dubitskiy. Physics of the Solid State. 66, 7, 1063 (2024).
[16] Y.V. Kislinskii, K.Y. Constantinian, I.E. Moskal, N.V. Dubitskiy, A.M. Petrzhik, A.V. Shadrin, G.A. Ovsyannikov. Russian Microelectronics **52**, Suppl 1, S53 (2023).
[17] A. Biswas, Y.H. Jeong. Curr. Appl. Phys. **17**, *5*, 605 (2017).
[18] K. Nishio, H.Y. Hwang, Y. Hikita. APL Mater. **4**, 036102 (2016).
[19] A. Gutierrez-Llorente, L. Iglesias, B. Rodrıguez-Gonzalez, F. Rivadulla. APL Mater. **6**, 091101 (2018).
[20] G.A. Ovsyannikov, K.I. Constantinian, G.D. Ulev, A.V. Shadrin, P.V. Lega, A.P. Orlov. Journal of Surface Investigation: X-ray, Synchrotron and Neutron Techniques. **18**, *1*, 210 (2024).
[21] A. Biswas, K.S. Kim, Y.H. Jeong. J. Appl. Phys. **116**, 21 (2014).
[22] T.J. Anderson, S. Ryu, H. Zhou, L. Xie, J.P. Podkaminer, Y. Ma, C.B. Eom. Appl. Phys. Lett. **108**, 15 (2016).
[23] D. Cui, Y. Xu, L. Zhou, L. Zhang, Z. Luan, C. Li, D. Wu. Appl. Phys. Lett. **118**, 5 (2021).
[24] L. Fruchter, O. Schneegans, Z.Z. Li. J. Appl. Phys. **120**, 7 (2016).
[25] L. Zhang, Q. Liang, Y. Xiong, B. Zhang, L. Gao, H. Li, Y.F. Chen. Phys. Rev. B **91**, *3*, 035110 (2015).
[26] H.C. Montgomery. J. Appl. Phys. **42**, *7*, 2971 (1971).
[27] W. Zhao, M. Gu, D. Xiao, Q. Li, X. Liu, K. Jin, J. Guo. Phys. Rev. Mater. **8**, *10*, 105001 (2024).
[28] S. Suresh, S.P.P. Sadhu, V. Mishra, W. Paulus, M.R. Rao. J. Phys.: Condens. Matter **36**, *42*, 425601 (2024).
[29] Yu.V. Kislinskii, G.A. Ovsyannikov, A.M. Petrzhik, K.Y. Constantinian, N.V. Andreev, T.A. Sviridova. Physics of the Solid State. 57, 12, 2519 (2015).
[30] V.A. Baydikova, N.V. Dubitskiy, I.E. Moskal, G.A. Ovsyannikov, A.M. Petrzhik, G.D. Ulev, K.Y. Constantinian, Yu.V. Kislinskii, A.V. Shadrin. Radioelectronics. Nanosystems. Information Technologies. **16**, *4*, 509 (2024).
[31] G. Rimal, T. Tasnim, G. Calderon Ortiz, G.E. Sterbinsky, J. Hwang, R.B. Comes. Phys. Rev. Mater. **8**, *7*, L071201 (2024).
[32] R. Choudhary, S. Nair, Z. Yang, D. Lee, B. Jalan. APL Mater. **10**, 9 (2022).
[33] N.K. Chumakov, I.A. Chernykh, A.B. Davydov, I.S. Ezubchenko, Y.V. Grishchenko, L.L. Lev, M.L. Zanaveskin. Semiconductors. **54**, *9*, 1150 (2020).
[34] D. Fuchs, A.K. Jaiswal, F. Wilhelm, D. Wang, A. Rogalev, M.L. Tacon. arXiv preprint arXiv:2502.02985 (2025).
[35] W. Surta, S. Almalki, Y.X. Lin, T. Veal, M. O'Sullivan. arXiv preprint:2406.01845 (2024).
[36] V. Fuentes, B. Vasić, Z. Konstantinovi; B. Martínez, L. Balcells, A. Pomar. J. Magn. Magn. Mater. **501**, 166419 (2020).

Translated by E.Ilinskaya